



Research on environmental dust pollution: ventilation and dust space–time evolution law of a fully mechanized mining face with 7-m mining height

Dawei Chen¹ · Wen Nie^{1,2} · Zihao Xiu¹ · Bo Yang¹ · Tao Du¹ · Qiang Liu¹ · Huitian Peng¹

Received: 15 April 2021 / Accepted: 2 December 2021 / Published online: 14 January 2022
© The Author(s), under exclusive licence to Springer-Verlag GmbH Germany, part of Springer Nature 2021

Abstract

To investigate the influence of dust produced by multi-dust sources at a fully mechanized mining face with a large mining height on the safety conditions in a coal mine, the No. 22305 fully mechanized mining face of the Bulianta coal mine was considered as the research object in this study, and the space–time evolution of dust was analyzed with computational fluid dynamics (CFD). The wind flow simulation results show that the distribution law of wind flow is mainly affected by the structure of the roadway, and the speed and direction of the wind flow change greatly while passing by corners and through large-scale equipment. The dust generation and pollution diffusion laws with respect to time and space were investigated based on simulations of dust production due to 5-s, 30-s, and 60-s coal cutting, continuous coal cutting, and hydraulic support shifting. The space–time evolution law under different dust-producing times shows the transportation and diffusion procedure of dust under the wind flow; the dust-generated via coal mining and shifting were superposed on the downwind side and a 36-m-long dust belt was formed, which filled the coal mining space; the dust concentration in the breathing zone 120 m downwind the front drum had a dust concentration higher than 1700 mg/m³, this was the crucial dust-proof area, and effective dust reduction methods should be addressed.

Keywords Coal mine environment · Fully mechanized mining face · Wind flow · Dust pollution · Dust space–time evolution law · Numerical simulation

Introduction

Occupational health problems in industrial production environments have received attention worldwide. According to the International Labor Organization, approximately 2.02

million people die from various occupational diseases each year, which is equivalent to an average of more than 5500 deaths per day (Elisaveta et al., 2010). In China, there have been nearly 1 million people diagnosed with occupational diseases, and more than 90% of these are occupational pneumoconiosis patients (Peng et al., 2019). There are approximately 30,000 new occupational disease cases in China each

Responsible editor: Philippe Garrigues.

✉ Wen Nie
niewen@sdust.edu.cn

Dawei Chen
sddadcdw@163.com

Zihao Xiu
xiu17839988621@163.com

Bo Yang
sddayang@163.com

Tao Du
dt970603@163.com

Qiang Liu
skdliuqiang2010@163.com

Huitian Peng
pht19920822@163.com

¹ College of Safety and Environmental Engineering, Shandong University of Science and Technology, Qingdao 266590, China

² State Key Laboratory of Mining Disaster Prevention and Control Co-Founded By Shandong Province and the Ministry of Science and Technology, Shandong University of Science and Technology, Qingdao 266590, China

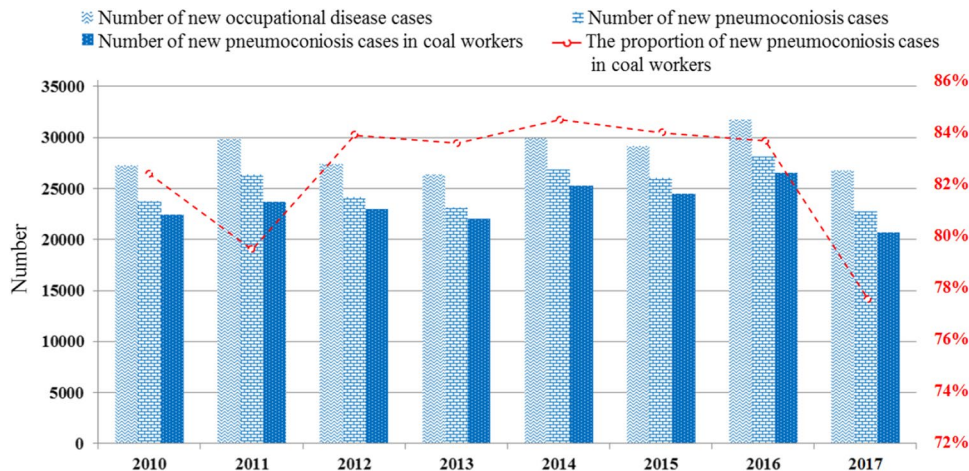
year (Fig. 1), 80% of which are linked to coal mine-related work (Cheng et al., 2016; Su et al., 2021; Lu et al., 2009). China's 7662 coal mines had provided approximately 3.5 billion tons of coal to the end of 2017 (Liu et al., 2019; Zhang et al., 2018a). Owing to the rapid development in the field of coal mine production and support equipment, the number of fully mechanized mining faces with large mining height has been increasing (Chen et al., 2018). The dust concentration would be as high as the point which was from 3000 to 5000 mg/m³ measured in working places underground coal mine, if sufficient and effective dust-suppression methods were not employed (Xie et al., 2010; Acton et al., 2011). The ultra-high dust concentration in the workplace can bring about outstanding occupational disease issues among workers (Zhang et al., 2014). In addition, a large amount of dust can damage equipment and cause malfunction. Workers who work in high dust concentrations for long periods of time are vulnerable to pneumoconiosis and eventually death. Scholars and researchers mainly used theoretical research, building a scaled-down actual model, field measurement, and numerical simulation to study the features of multi-dust pollution and diffusion laws in coal mine (Chen et al., 2018). For instance, Xu et al. (2014) performed numerical simulations and field measurements to obtain the characteristics of a coal mine ventilation system and to study the movement patterns of dust production due to coal cutting and hydraulic support shifting. Pang et al. (2017) and Xu et al. (2018) analyzed the measured of the dust concentrations of a fully mechanized mining face in a coal mine to determine the distribution range and quality of respirable dust and total dust. They proved that the both coal cutting and hydraulic support shifting are the most important dust sources in the underground. Sun et al. (2018) investigated the disturbance intensity and effect of gas turbulence in coal mines on dust diffusion. According to the comparative analysis, the turbulent wind flow generated by the interaction between coal cutting and original ventilation system is the most significant

factor affecting the dust distribution. Gómez and Milioli (2003) conducted a two-dimensional riser numerical simulation research and verified the numerical simulation results through specific experiments. Many studies and researches have fully proved the reliability of numerical simulations for this case. It can not only accurately calculate the flow field distribution and particle diffusion laws by simulating the motion state of wind flow and solid particles, but also can save a lot of manpower and material resources under the condition of ensuring data reliability (Krawczyk, 2020; Wang et al., 2018). Therefore, numerical simulations are widely used in the fields of fluid dynamics, rock mechanics, and thermodynamics.

Scholars worldwide have determined the characteristics of and mitigation methods for dust pollution in coal mines (Chang et al., 2020; Seaman et al., 2020). Yao et al. (2015) used a gas-phase multiphase flow mathematical model to simulate dust diffusion and analyzed optimal dust exhausting wind speed of steeply inclined fully mechanized mining face. Ansart et al. (2009) developed a numerical simulation method to investigate the distribution law of coal mine dust. Zhou et al. (2016) analyzed the impact of wind flow on the respirable dust migration law at a 5.6 m high at a fully mechanized mining face. However, the applied physical models are too simplified (Zhou et al., 2017), they usually only include mining sections, simplified internal coal mining machines, and hydraulic supports, and ignore the infiltration of wind and dust due to incomplete models and production systems. The results of numerical simulation studies have qualitatively been analyzed, but there were no detailed, quantitative analyses of the simulation process have been presented.

According to the conclusions of the paper. (I) Because coal mine workers usually work at the coal cutter and under the shifted hydraulic support, the impact of coal cutting and hydraulic support shifting on the personnel breathing zone (i.e., the horizontal space in which the human nose

Fig. 1 New cases of occupational diseases in recent years



and mouth usually are, which corresponds to a height of 1.55–1.75 m in the vertical space) during the dust production was analyzed. (II) The physical model is based on an actual coal mine environment, the physical model, which included two main dust sources—coal cutting and hydraulic support shifting—was composed of four parts: a coal mining area, an air inlet lane, a return airway, and goaf. In the meantime, the physical model of research restores the layout of equipment in the fully mechanized mining face with a large mining height. (III) FLUENT was adopted for the numerical simulation software, while CDF-POST was used for processing and displaying numerical simulation results Furthermore, by considering the impacts of the arrangement of the large-scale support, coal mining, and transfer equipment on the wind flow, further quantitative analysis of the dust pollution diffusion law was conducted. (IV) The main objective of this research is investigating the evolution of coal mine dust in space and time, performing a specific description of the complete mining procedure, from dust generation, to transport, and removal via the roadway.

Model construction and meshing

Mathematical model

CFD simulations are performed to determine the laws of different flow phenomena to solve fundamental control equations (Torano et al., 2011). In this research, the fresh wind flow in the roadway is described as a gas phase, and the dust particles produced by the two main dust sources (coal cutting and hydraulic support shifting) are described as the solid phase. This study used the standard $k-\epsilon$ model to simulate the turbulent continuous phase wind flow in a fully mechanized coal mining face with large mining height (Cheryl et al., 2009). By considering the dust particles as discrete phases, the combination of the $k-\epsilon-\Theta$ - k_p model was employed to calculate the wind flow-dust turbulent flow in the two-phase coal mining space (Kong et al., 2017; Hu et al., 2016).

Specifically, the commonly used Reynolds-averaged Navier–Stokes method was applied. The time average of any variable ϕ is defined as follows (Zhang et al., 2018b):

$$\bar{\phi} = \frac{1}{\Delta t} \int_t^{t+\Delta t} \phi(t) dt \tag{1}$$

where the superscript “–” of ϕ represents the time-averaged value. If the superscript “’” represents the pulsation value, the relationship between the instantaneous value of the physical quantity ϕ , the time average value $\bar{\phi}$, and the pulsation value ϕ' is as follow: $\phi = \bar{\phi} + \phi'$, $\overline{\phi\phi'} = 0$, $\overline{\phi'} = \bar{\phi}$, $\overline{\phi'^2} = 0$.

The turbulent gas-phase and discrete particle-phase equations are as follows (Gousseau et al., 2011; Liu et al., 2018b):

Continuous equation of turbulent gas phase:

$$\frac{\partial(\alpha\rho)_q}{\partial t} + \frac{\partial(\alpha\rho U_i)_q}{\partial x_i} = -\frac{\partial}{\partial x_i} \left[\overline{(\alpha\rho)'_q U'_{i,q}} \right] \tag{2}$$

Continuous equation of particle phase:

$$\frac{\partial(\alpha\rho)_p}{\partial t} + \frac{\partial(\alpha\rho U_i)_p}{\partial x_i} = -\frac{\partial}{\partial x_i} \left(\overline{(\alpha_p\rho_p)' U'_{i,p}} \right) \tag{3}$$

where q – gas phase; p – particle phase; ρ – gas phase density (kg/m^3); α – the volume fraction of gas phase in the control volume; U – velocity vector (m/s); t – time (s); i – the indicator sign of the tensor.

The momentum equation describing the gas phase in the numerical simulation is as follows (Patel et al., 2017):

$$\begin{aligned} \frac{\partial(\alpha\rho U_i)_q}{\partial t} + \frac{\partial(\alpha\rho U_i U_j)_q}{\partial x_j} = & -\alpha_q \frac{\partial P}{\partial x_j} + \alpha_q \rho_q g_j + \frac{\partial \tau_{ij}}{\partial x_i} \\ & + \beta_j (U_{j,p} - U_{j,q}) - \frac{\partial}{\partial x_i} \left(\alpha_q \rho_q \overline{U'_{i,q} U'_{j,p}} \right) \end{aligned} \tag{4}$$

where the Reynolds stress is $\tau_{ij} = \mu_q \left[\left(\frac{\partial U_{j,q}}{\partial x_i} + \frac{\partial U_{i,q}}{\partial x_j} \right) - \frac{2}{3} \delta_{ij} \frac{\partial U_{l,q}}{\partial x_l} \right]$.

The momentum equation describing the particle phase in the numerical simulation is as follows (Peirano et al., 2001):

$$\begin{aligned} \frac{\partial(\alpha\rho U_i)_p}{\partial t} + \frac{\partial(\alpha\rho U_i U_j)_p}{\partial x_j} = & -\alpha_p \frac{\partial P}{\partial x_j} + \rho_p g_j + \frac{\partial \Pi_{ij}}{\partial x_i} \\ & + \beta_j (U_{j,q} - U_{j,p}) - \frac{\partial}{\partial x_i} \left(\alpha_p \rho_p \overline{U'_{j,p} U'_{i,p}} \right) \\ & - \frac{\partial}{\partial x_i} \left(\overline{U_{j,p} (\alpha_p \rho_p)' U'_{i,p}} + \overline{U_{i,p} (\alpha_p \rho_p)' U'_{j,p}} \right) \end{aligned} \tag{5}$$

When $\Pi_{ij} = \bar{\Pi}_{ij}$

$$\begin{aligned} \Pi_{ij} = & -P_p + \xi_p \delta_{ij} \frac{\partial U_{m,p}}{\partial x_m} + \mu_p \left[\left(\frac{\partial U_{j,p}}{\partial x_i} + \frac{\partial U_{i,p}}{\partial x_j} \right) - \frac{2}{3} \delta_{ij} \frac{\partial U_{m,p}}{\partial x_m} \right] \\ = & -P_p + \left(\xi_p - \frac{2}{3} \mu_p \right) \delta_{ij} \frac{\partial U_{m,p}}{\partial x_m} + \mu_p \left(\frac{\partial p}{\partial x_i} + \frac{\partial U_{i,p}}{\partial x_j} \right) \end{aligned} \tag{6}$$

The temperature equation describing the particle phase in the numerical simulation is as follows:

$$\begin{aligned} \frac{3}{2} \left[\frac{\partial}{\partial t} (\alpha\rho\Theta)_p + \frac{\partial}{\partial x_i} (\alpha\rho U_i \Theta)_p \right] = & \Pi_{ij} \frac{\partial U_{j,p}}{\partial x_i} + \frac{\partial}{\partial x_i} \left[\Gamma_\Theta \frac{\partial \Theta}{\partial x_i} \right] - \gamma - \frac{3}{2} \alpha_p \rho_p \overline{U'_{i,p} \Theta} \\ & - \frac{3}{2} \frac{\partial}{\partial x_i} \left(\overline{\Theta (\alpha_p \rho_p)' U'_{i,p}} + \overline{U_{i,p} (\alpha_p \rho_p)' \Theta'} \right) \end{aligned} \tag{7}$$

In Eqs. (4)–(7), j, l -the indicator sign of the tensor; P, P_p – the gas phase pressure and particle phase pressure (Pa); β_j –

the drag coefficient along the direction of j ; γ —the collision energy dissipation; τ —the shear force (N/m^3); ξ_p —the particle phase viscosity; $\delta_{i,j}$ —the “Kronecker delta” symbol; μ —the viscosity coefficient of the laminar flow ($\text{Pa}\cdot\text{s}$); Θ —temperature (K); Γ_Θ —the particle temperature transport coefficient.

The turbulence energy equation (i.e., the k equation) describing the gas phase in the numerical simulation is as follows:

$$\frac{\partial}{\partial t}(\alpha_q \rho_q k) + \frac{\partial}{\partial x_j}(\alpha_q \rho_q U_{j,q} k) = \frac{\partial}{\partial x_j} \left(\frac{\mu_e}{\sigma_k} \frac{\partial k}{\partial x_j} \right) + G_k + G_p - \alpha_q \rho_q \varepsilon \quad (8)$$

The turbulence dissipation rate (i.e., the ε equation) describing the gas phase in the numerical simulation is as follows (Pontiggia et al., 2009):

$$\frac{\partial}{\partial t}(\alpha_q \rho_q \varepsilon) + \frac{\partial}{\partial x_j}(\alpha_q \rho_q U_{j,q} \varepsilon) = \frac{\partial}{\partial x_j} \left(\frac{\mu_e}{\sigma_\varepsilon} \frac{\partial \varepsilon}{\partial x_j} \right) + \frac{\varepsilon}{k} [C_1(G_k + G_p) - C_2 \alpha_q \rho_q \varepsilon] \quad (9)$$

$$G_k = m_{q,t} \left(\frac{\partial U_{i,q}}{\partial x_j} + \frac{\partial U_{j,q}}{\partial x_i} \right) \frac{\partial U_{i,q}}{\partial x_j}; G_p$$

$$\text{where } = \frac{2\alpha_p \rho_p}{\tau_p} \left(C_p^v \sqrt{k(k_p + \Theta)} - k \right); \mu_e = \mu_q + C_\mu \alpha_q \rho_q \frac{k^2}{\varepsilon}$$

The viscosity of the gas phase turbulent flow in the Eq. (2) due to turbulent flow is closed by the k_p model of the gas phase and the turbulent flow of the particle phase is k_p modeled as follows: $k_p = \frac{1}{2}(U'_{i,s} U'_{t,s})$, i.e., the velocity pulsation energy of the particle caused by the turbulence mechanism (Wang et al., 2018, 2016).

The turbulent energy equation describing the particle phase in the numerical simulation is as follows (Wang et al., 2009; Liu et al., 2018a).

$$\frac{\partial}{\partial t}(\alpha_p \rho_p k_p) + \frac{\partial}{\partial x_k}(\alpha_p \rho_p U_{p,k} k_p) = \frac{\partial}{\partial x_k} \left(\frac{\mu_{p,t}}{\sigma_\varepsilon} \frac{\partial k_p}{\partial x_k} \right) + G_{kp} - \alpha_p \rho_p \varepsilon_p + \frac{\partial}{\partial x_k} \left(k_p \frac{\mu_{p,t}}{\sigma_\varepsilon} \frac{\partial \alpha_p \rho_p}{\partial x_k} \right) \quad (10)$$

In Eqs. (8)–(10), ε —the dissipation rate of turbulence; k —the kinetic energy of turbulence; G_k —the production term of turbulent kinetic energy k ; τ —the shear force; σ_k , σ_ε —the turbulence Prandtl number of k equation and ε equation; the empirical constants in the formula are $C_1 = 1.44$, $C_2 = 1.92$, $C_p^v = 0.85$, $C_\mu = 0.09$.

After being closed by the above model, it should be mentioned that the model neglects the impact of solid turbulence on the particle temperature equation and gas-particle drag force in the two-phase flow in the three-dimensional turbulence space (Nie et al., 2017; Widiatmojo et al., 2015; Cai et al., 2018).

Dust particles are influenced by different forces in a turbulent flow field (Cundall and Strack, 2008):

$$\frac{d\vec{u}_p}{dt} = F_D(\vec{u} - \vec{u}_p) + \frac{g(\rho_p - \rho)}{\rho_p} + \vec{F}_{vm} + \vec{F}_p + \vec{F}_{mag} + \vec{F}_{saf} + \vec{F}_{other} \quad (11)$$

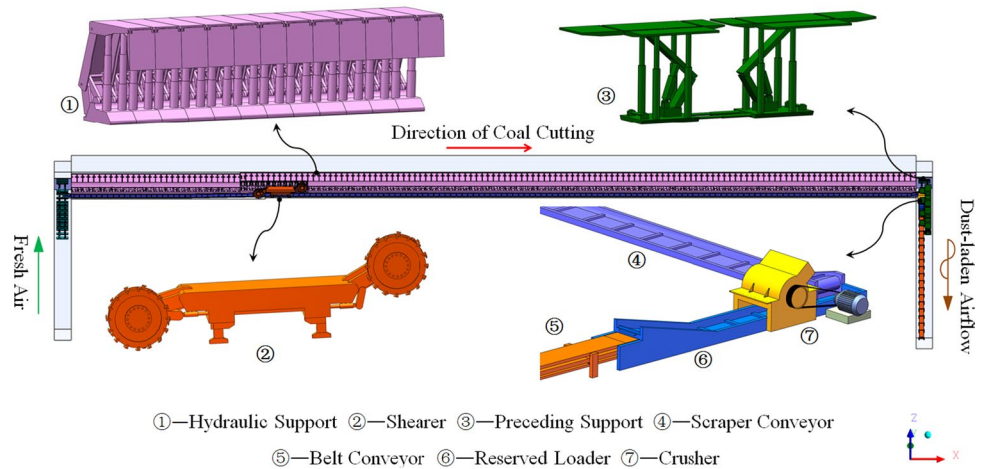
where \vec{u} —air velocity (m/s); \vec{u}_p —particle velocity (m/s); $F_D(\vec{u} - \vec{u}_p)$ —the drag force on particle with unit mass (N); $\frac{g(\rho_p - \rho)}{\rho_p}$ —the sum of the gravity and buoyancy on particle with unit mass (N); \vec{F}_{vm} —virtual mass force (N); \vec{F}_p —pressure gradient force (N); \vec{F}_{mag} —magnus lift force (N); \vec{F}_{saf} —saffman lift force (N); \vec{F}_{other} —the force of particle collisions (N).

Physical model introduction

Using the No. 22305 fully mechanized mining face of the Bulianta coal mine as the research object, SolidWorks was employed to build a full-scale physical model, which comprised the material roadway, the coal mining area, goaf, and the transportation roadway. Figure 2 shows that the physical model is located in the coordinate system. All the roadways adopt regular rectangular sections. The coal mining area was $300.8 \text{ m} \times 8.0 \text{ m} \times 6.8 \text{ m}$. The material roadway was $110.0 \text{ m} \times 6.0 \text{ m} \times 4.3 \text{ m}$. The transportation roadway was $116.0 \text{ m} \times 5.8 \text{ m} \times 4.5 \text{ m}$ and the goaf was $300.8 \text{ m} \times 12.0 \text{ m} \times 6.8 \text{ m}$. According to the Bulianta coal mine operational procedure, we adopted the exact geological conditions around the coal mine and the 8- to 15-m periodic caving span at the working face. It is reasonable to set the width of the goaf to 12 m. The double-drum coal cutter performs round-trip coal cutting activities in the coal mining area; hence, its position is relatively flexible. It is located at 69.5 m on the downwind side of the air-entrance corner. We also built 150 hydraulic division supports, 2 advanced supports, 1 scraper conveyor, and 1 set of broken, transfer, and transport equipment according to the actual situation. This study endeavored to restore the overall layout of the coal mining system and transportation system in the fully mechanized mining face with large mining height, in order to minimize the deviation of the physical model from the numerical simulation results.

Meshing and grid independence analysis

The physical model was prepared with SolidWorks software and outputted as a Parasolid(*.x_t) file, which was then imported into ICEM for meshing. Firstly, in the process of spatially dividing the calculation area, ICEM was able to merge the sharp endpoints on the model geometry, and automatically ignore the small model defects. Then, the unstructured grid was generated. Since the grid quality played a crucial role in numerical simulation results (Camelli et al., 2014; Yao et al., 2013), it was of necessity to smooth the elements and remove the low-quality elements (element quality is less than 0.4) to improve grid quality.

Fig. 2 Physical model diagram

In this study, a grid containing 6,439,374 elements was first generated. The grid independence must be checked before the formal numerical simulation to avoid discrepancy in the numerical simulation with the change of grid density (Wang et al., 2020). Therefore, two other grids containing 8,567,562 elements and 5,047,405 elements were generated by changing the maximum and minimum element size. Since wind flow is an important factor affecting dust diffusion, numerical simulations of wind flow were performed to verify the grid independence for the three grids with different number of elements. The elements of three grids were 8,567,562 elements, 6,439,374 elements, and 5,047,405 elements. Figure 3 presents the actual field wind flow measurement data to assess the reliability of the simulated wind flow. The wind flow measurements were performed with a TSI-9545 wind meter. The wind flow speed was measured at 10-m intervals from the air inlet and the measured data of three measurements were averaged.

Figure 3 shows the evidently different elements number of the three grids. However, the difference in the elements number does not affect the wind flow simulation data. Therefore, the three grids meet the requirements of simulation. Moreover, the actual measured wind flow data were compared with the simulation data of the three grids; the relative error bars were set to $\pm 20\%$ of the actual measured data because the study is a practical engineering problem. The three folding lines all fall within the error bars of the measured data; most errors are below 10%, which means that the simulation data of the three schemes are in good agreement with the actual measured data.

In summary, the three grids can be used for further simulations. After considering the calculation time and simulation result files size, the grid with 6,439,374 elements for the numerical simulations was determined finally. The maximum and minimum elements in the grid were 0.998927 and 0.086538; the overall elements indicate that the high-quality elements are greater than 98%, which can be used

for the next step of numerical simulation. The grid quality is shown in Fig. 4. In addition, the number of elements is shown in Table 1.

Numerical simulations

Parameters for numerical simulations

The main parameters of the numerical simulation were set according to the basic principles of fluid dynamics and analysis result of the wind flow and dust data collected at the production site, as shown in Table 2.

The number of large, mechanized equipment and its complex structure at the 7 m-high fully mechanized mining face have an evident impact on the wind flow distribution. Furthermore, the wind flow plays an important role in transporting dust in the roadway. The numerical simulation of wind flow is crucial for numerically simulating the behavior of dust. Therefore, it was necessary to confirm the convergence of the wind flow simulation had to be confirmed before determining the migration law of the discrete-phase dust. In order to display intuitively the wind flow speed streamline, dust traces, and dust concentration distribution, the transparent treatment function of CFD-POST was used for the hydraulic support top beam in the physical model.

Simulation of wind flow in a 7-m-high fully mechanized mining face

For the purpose of clearly and intuitively display the wind flow speed and the trend of the wind flow in a fully mechanized mining face, the rainbow column was set to a minimum value of 0 m/s and a maximum value of 2.5 m/s, while the density of the track is adjusted. Red represents the case in which the speed exceeded 2.5 m/s.

Fig. 3 Grid independence analysis and wind flow measurement

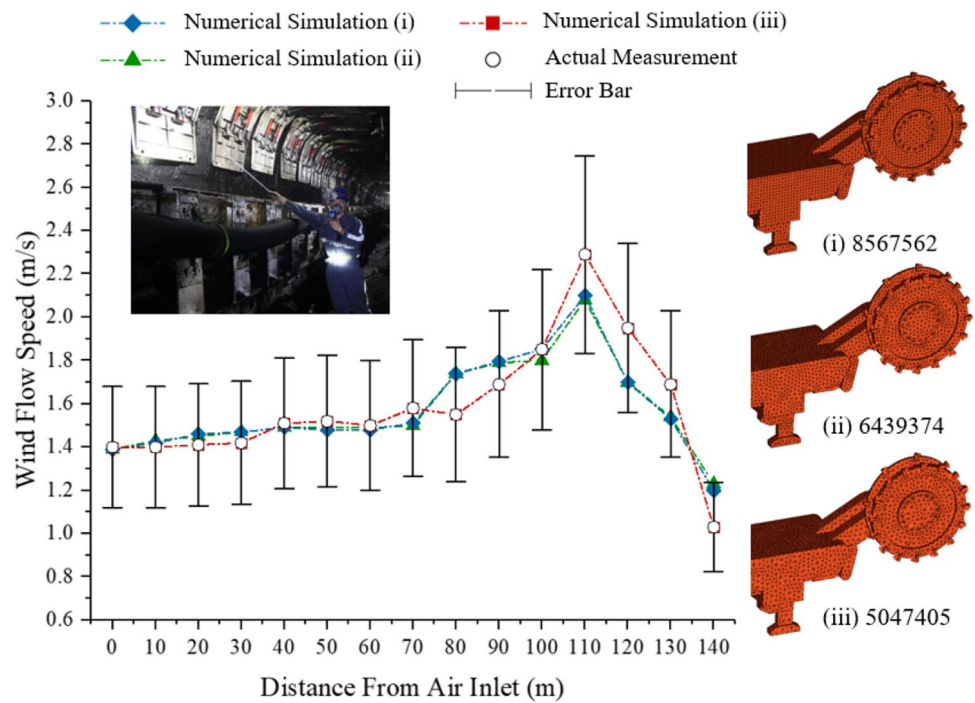


Fig. 4 Grid quality

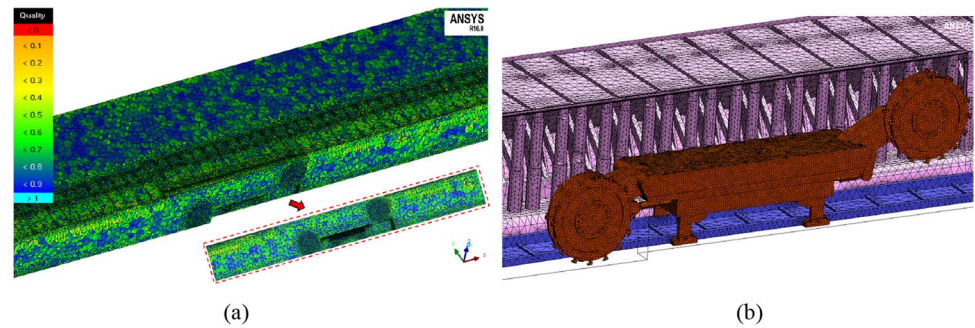


Table 1 The number of elements in the grid

Elements quality range	Number of elements	Proportion	Elements quality range	Number of elements	Proportion
0.0–0.05	16	0.000%	0.50–0.55	478,918	7.437%
0.05–0.10	137	0.002%	0.55–0.60	505,843	7.855%
0.10–0.15	824	0.013%	0.60–0.65	471,534	7.323%
0.15–0.20	3492	0.054%	0.65–0.70	475,938	7.391%
0.20–0.25	11,386	0.177%	0.70–0.75	417,151	6.478%
0.25–0.30	29,139	0.453%	0.75–0.80	428,962	6.662%
0.30–0.35	15,023	0.233%	0.80–0.85	504,874	7.840%
0.35–0.40	25,608	0.398%	0.85–0.90	530,792	8.243%
0.40–0.45	325,049	5.048%	0.90–0.95	1,022,601	15.880%
0.45–0.50	678,569	10.538%	0.95–1.00	513,518	7.975%
Total elements of the grid				6,439,374	

Table 2 Parameter setting

Project	Setting	Project	Setting
Turbulent model	Standard <i>k-ε</i> model	Material	Coal-hv
Inlet airflow velocity	1.4 m·s ⁻¹	Dust sources	Coal cutting/hydraulic support shifting
Inlet boundary	Velocity-inlet	Minimum particle diameter (m)	8.00e-07/7.00e-07
Outlet boundary	Pressure-outlet	Median particle diameter (m)	4.30e-06/3.00e-05
Particle model	Discrete phase model	Maximum particle diameter (m)	2.00e-04/8.00e-05
Solution methods	SIMPLE	Maximum iterative steps	50,000
DPM iterative steps of the continuous phase	100	Diameter distribution	Rosin-Rammler
Under-relaxation factor	0.01	Diffusion parameter	1.13

Figure 5 shows that in the wind direction along the working surface; the section was regular and unobstructed within 82 m from the material roadway inlet. The inlet wind flow speed remained at 1.4 m/s without significant change. The flow velocity increased to values between 1.6 and 2.0 m/s as it flowed through the single hydraulic support. Due to a windshield being set at the air-entrance corner, the wind flow changed obviously as it passed by the corner. Because of the centrifugal force, the wind flow speed near the outer corner side exceeded that near the inner corner side. The wind flow speed increased instantaneously at the air-entrance corner, exceeding 2.5 m/s, and the maximum wind flow speed was twice the inlet wind flow speed. At this time, some wind flow entered the goaf and spiraled forward at 0.5 m/s. The

advancing support was 6 m on the windward side of the coal cutter, and the step distance of the hydraulic support was 0.86 m. After the wind flow had entered the coal mining area, it mainly accumulated in the haulageway (i.e., the route through which the coal cutter passed through), and the wind flow speed was kept at 0.9 m/s. The large, high mining space allowed the wind to flow through the section sufficiently. When the wind flow passed through the coal cutter, its speed increased slightly to values between 1.1 and 1.2 m/s.

The wind flow in the untouched area presented an evident decrease-increase pattern. The wind flow in the wide non-advancing support area was relatively stable. However, because of the blockage of surrounding objects, the wind speed was slowly reduced, the wind flow speed in the

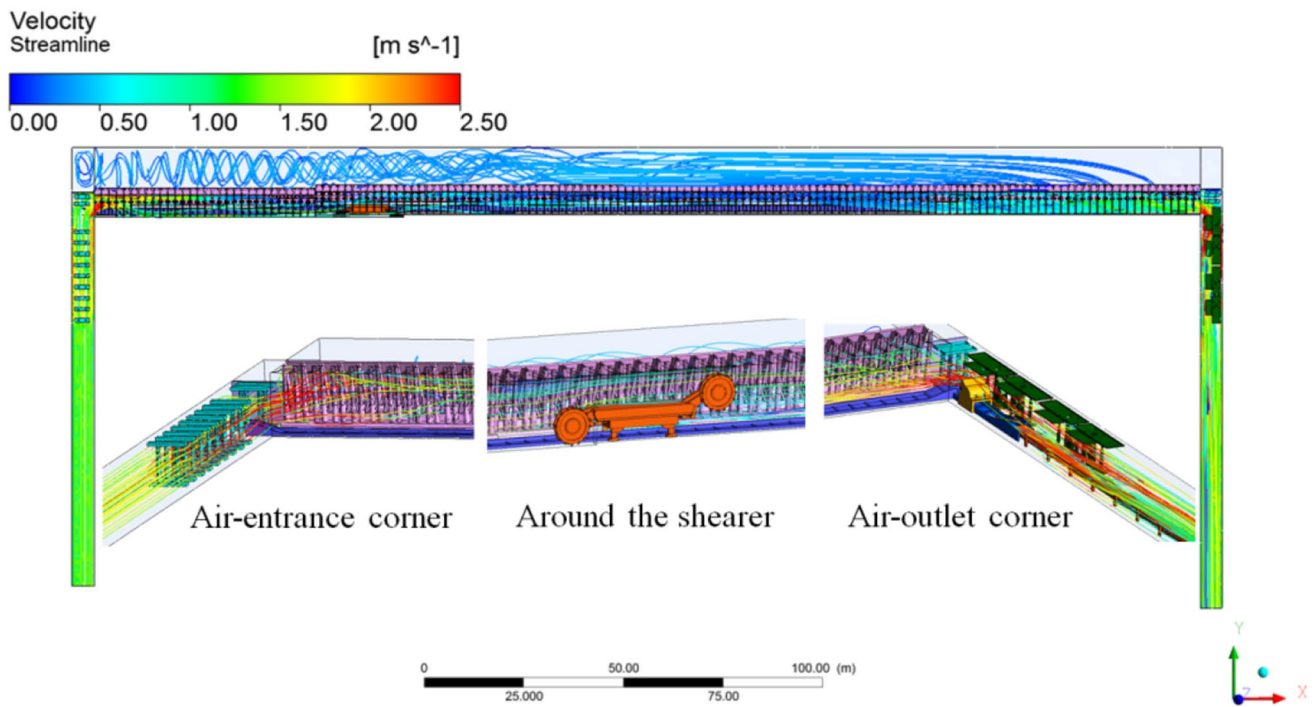


Fig. 5 Wind flow speed streamline diagram

haulageway gradually decreased to 0.7 m/s, and the wind flow speed on the sidewalk decreased to 0.3 m/s. Subsequently, part of the wind flow in the goaf area 180 m to the downwind side of the coal cutter re-entered the non-advancing support area, and the total wind flow speed rose back to 1.4 m/s, which then increased rapidly to above 1.9 m/s at 26 m before the return wind corner.

After the wind flow had entered the return air roadway through the return wind corner, large equipment such as the lead bracket, the transfer machine, and the crusher occupied most of the space of the roadway, so the flow cross section was narrow, and the wind flow was disordered and maintained a speed of more than 2.2 m/s. After the wind passed through the second lead bracket, the section enlarged, and there was less equipment, so the wind flow speed decreased to 1.3 m/s. At this time, the wind flow speed away from the conveyor-belt side reached 1.6 m/s, slightly higher than that near the conveyor belt.

According to Figs. 6 and 7, the wind flow from the bottom plate to the top plate showed a low–high–low distribution trend. The overall wind flow speed in the haulageway was higher than that in the goaf. The high-speed wind flow of the air-entrance corner filled the entire vertical space, and the wind flow speed in the middle and lower parts of the vertical space in the return wind corner was significantly higher than that in the upper space. The air leakage of the goaf flowed into the goaf from the air-entrance corner and advanced spiraling at 0.4 m/s speed. At the corresponding coal cutter, owing to the lateral wind flow, part of the sidewalk wind flow leaked into the goaf, disturbing the wind flow in the goaf. Because of this high-speed air leakage, the original spirally advancing wind flow gradually stabilized and remained at 0.5–0.6 m/s, which then dropped to less than 0.3 m/s at the end of the goaf; finally, the wind began to flow back to the sidewalk and the haulageway.

According to Figs. 8 and 9, the height of the sidewalk breathing zone was approximately 1.55 m. However, because of the hydraulic support base with 0.7 m height and the height of the workers, 2.2–2.4-m height

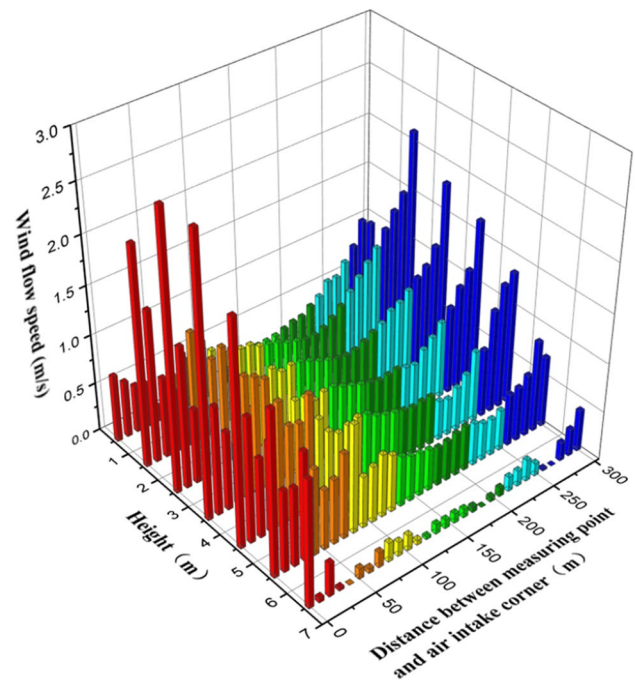


Fig. 7 Distribution of wind flow speeds at different heights in the three-dimensional haulageway

was chosen for analysis. Because the height of the large mining was 6.8 m, the wind flow trends were similar in the selected height range. Due to the sudden increase in wind flow speed at the air-entrance corner, the wind flow speed on the sidewalk breathing zone could reach more than 1.8 m/s and decreased to a minimum (0.3 m/s) 160 m to the downwind side of the air-entrance corner. While approaching the return wind corner, the wind flow began to return with that in the goaf, and the wind flow speed of the sidewalk breathing zone slowly increased to 0.8 m/s. In the vertical three-dimensional space, the wind flow speed gradually decreased as height increased at the same position on the sidewalk of the mining area.

Fig. 6 Wind flow speed cloud diagram for different height sections in three-dimensional space

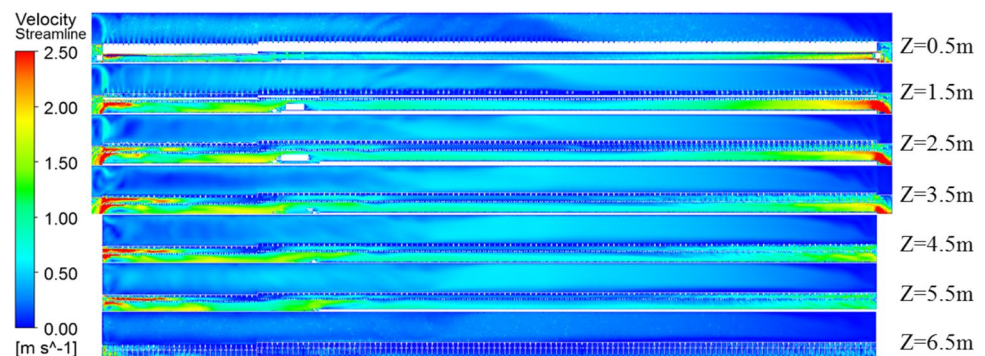


Fig. 8 Histogram of the sidewalk breathing-zone height wind flow speed data

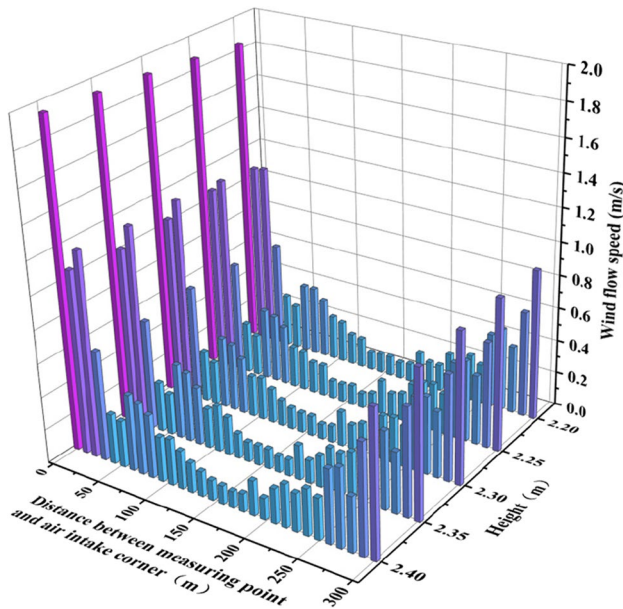
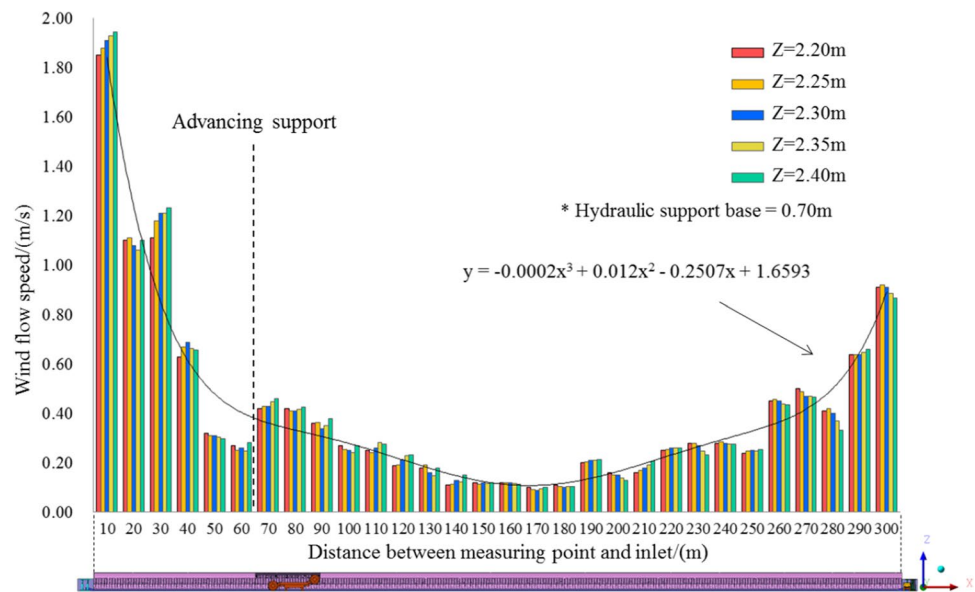


Fig. 9 Distribution of wind flow speed of the sidewalk breathing zone in the coal mining area

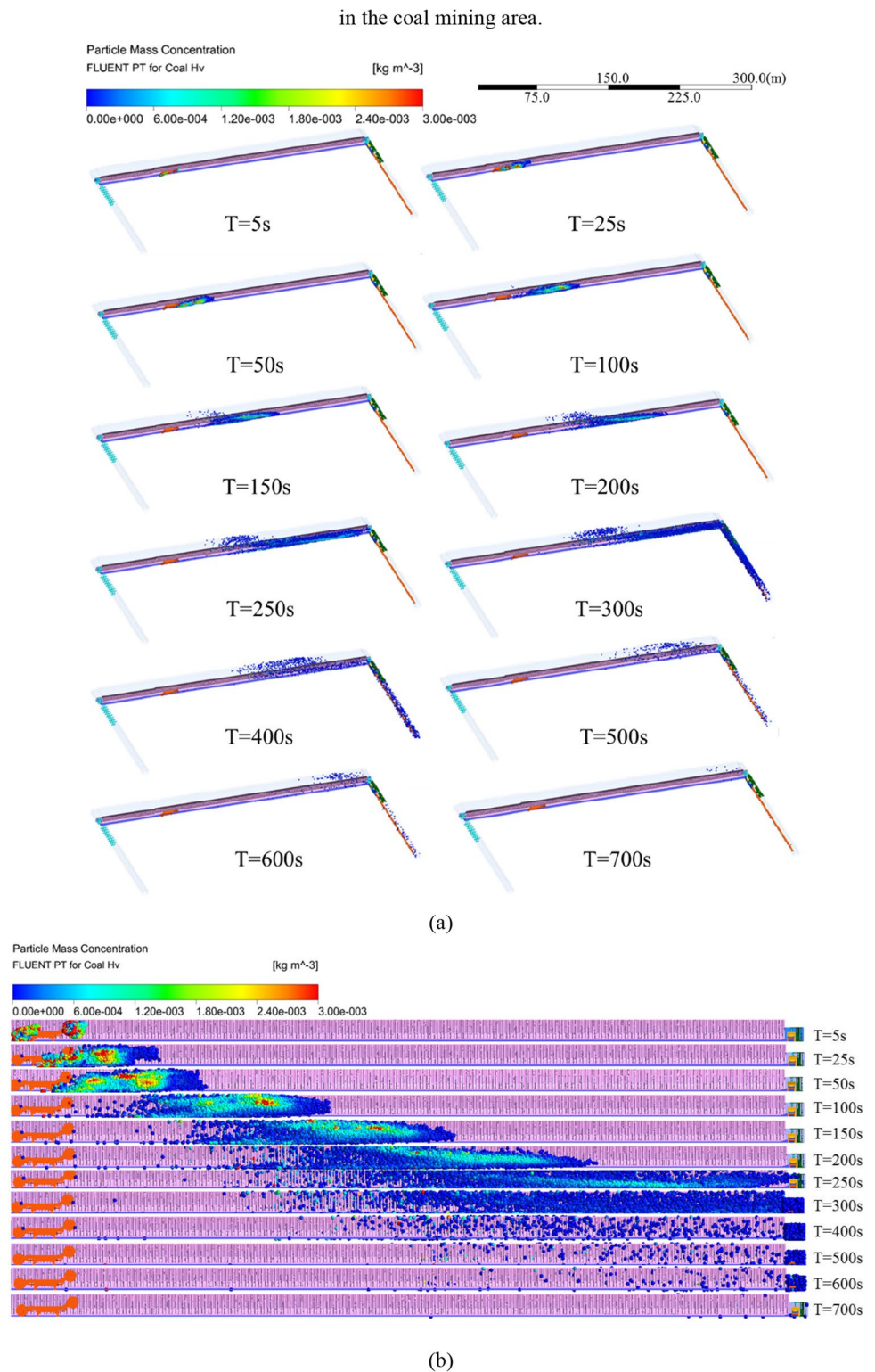
Numerical simulation of the space–time evolution law of dust at 7-m-high fully mechanized mining face

In accordance with the wind flow simulation results, the time scale was considered transient. Combined with dust particle distribution and roadway transparency treatment, the effects of different dust generation durations during mining operations at a fully mechanized mining face and the space–time

evolution of dust pollution diffusion during continuous operation were analyzed.

As shown in Fig. 10, during $T=5–25$ s, the dust generated by the rear drum moved close to the coal wall with the wind flow, and the dust generated by the front drum diffused in a vertical direction; when $T=50$ s, dust generated by the front and rear drums started to overlap, and moved to the downwind side. At this time, most of the dust was concentrated between the coal cutter and the coal wall; at $T=100$ s, because the wind flow speed within 180 m of the coal cutter side of the coal cutter was stable at 0.7–1.0 m/s, the dust from the front and rear drum gathered into a dust cloud of 46-m length, with a high concentration at the center and a lower surrounding concentration. The dust particles in the front received a high amount of kinetic energy; the speed exceeded 0.96 m/s. When $T=150$ s, at 28 m downwind of the coal cutter, the dust cloud filled the coal wall to the sidewalk space, while the center concentration gradually decreased, and the dust pollution distance gradually increased. The dust particles moved laterally into the goaf due to continuous collisions; during $T=200–250$ s, during this time, the dust concentration was below 600 mg/m^3 , and the dust particles at the front end of the dust mass were close to the return wind corner; when $T=300$ s, the dust entered the return air roadway. Because the wind flow speed of the return airway exceeded 1.2 m/s, the dust at the front began to exit the roadway. The dust pollution distance was currently up to 332 m. During $T=300–500$ s, the dust in the room between the coal wall and the sidewalk maintained a speed of above 0.7 m/s, and continuously went in to the transportation roadway, accelerating the movement out of the roadway. The dust continuously migrated to the downwind side with the wind flow, and the particles and the dust started to flow

Fig. 10 Laws of dust pollution diffusion in coal cutting for 5 s



back into the haulageway at $T=400$ s. When $T=600\text{--}700$ s, the dust in the goaf completed returning and left the roadway. When $T>700$ s, a small part of the remaining dust in the goaf was retained in the no-flow corner, and gradually settled due to the action of gravity.

As shown in Fig. 11, at $T=30$ s, the front and rear drums produced the large quantity of the dust, which filled the room near the coal cutter and then spread to the sidewalk area. When $T=50$ s, affected by the lateral wind flow at the rear drum of the coal cutter and the collisions among the dust

particles, a small amount of dust in the sidewalk leaked into the goaf from the lower gap of the hydraulic support and diffused into the whole space. During $T=100\text{--}150$ s, the dust in the haulageway moved backward with the wind flow, at a speed of above 0.7 m/s. Due to the continuous expansion of the dust pollution area, the dust concentration decreased continuously. When $T=200\text{--}300$ s, all of the dust in the haulageway and the sidewalk entered the return airway and moved out of the roadway. It was observed that the dust in the goaf began to flow back into the haulageway with the wind flow. During $T=400\text{--}700$ s, the dust in the goaf completed returning and left the roadway. When $T>800$ s, the remaining small amount of dust in the goaf was retained in the no-flow corner, and gradually settled due to gravity.

As shown in Fig. 12, the dust migration and diffusion speed were significantly reduced, and the large quantity of dust particles collided with each other, which affected their migration tracks along with the wind flow. Thus, a great quantity of dust particles remained in the coal mining area and impacted the environment. When $T=60$ s, the coal dust from the front and rear of the coal cutter filled the space between the coal wall to the sidewalk and diffused into the goaf from the lower gap of the hydraulic support, affected by the lateral wind flow at the rear drum with a speed of 0.8 m/s. When $T=100$ s, the dust moved down to the wind side, and the concentration of the central decreased rapidly. Affected by the spiral leakage of 0.4 m/s, the dust in the goaf first adhered to the wall and then gradually diffused on the cross section of the whole goaf due to the interaction of dust particles; When $T=200\text{--}500$ s, the dust entered the return airway and started to exit the roadway. At this time, the concentration of dust decreased due to the large distribution range. When $T=700$ s, most of the dust in the haulageway and sidewalk had been removed from the roadway. The dust in the goaf began to flow back with the wind flow into the haulageway with the wind flow. During $T=700\text{--}900$ s, the dust in the goaf completed returning and left the roadway; when $T>900$ s, the remaining small amount of dust in the goaf was retained in the no-flow corner, and gradually settled due to gravity.

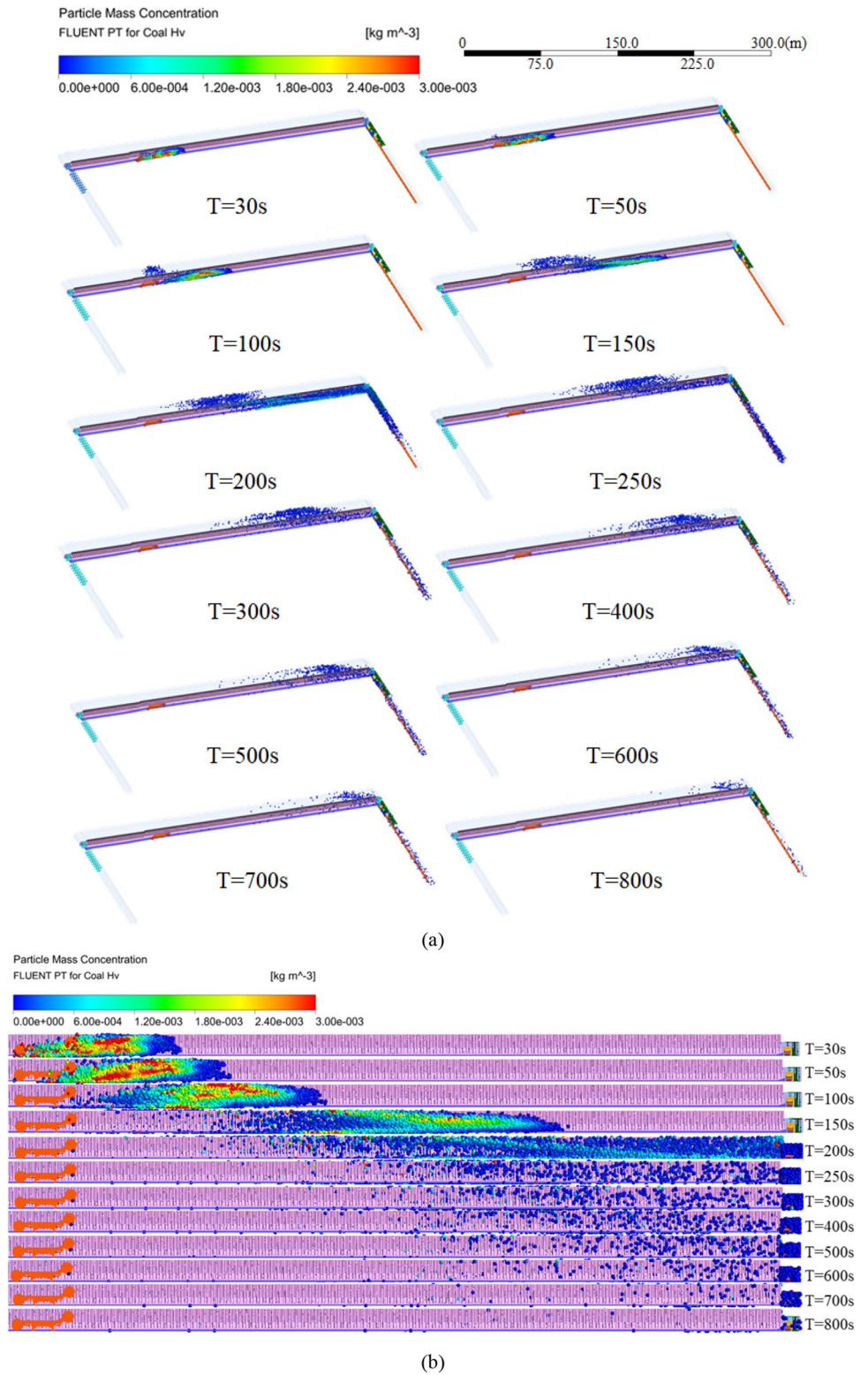
As shown in Fig. 13 that, when $T=10$ s, the rear drum dust moved backward, and the front drum dust spread rapidly and vertically. The hydraulic support began to move as the hydraulic support top-beam left the top plate, and a small amount of dust immediately leaked into the mining area along the gap. When $T=30$ s, two to three sets of hydraulic supports began to enter the shifting state. The phenomenon of dust falling along the coal block caused the moving dust to spread vertically, and some other dust spread to the wind side with the wind. The coal-cutting dust quickly filled the coal mining space in both horizontal and vertical directions. When $T=50$ s, a small amount of moving dust entered the goaf, and other dust was mixed with the coal-cutting dust

and transported to the downwind side in the haulageway. Owing to the high concentration of dust accumulation on the floor of the roadway, the dust concentration distribution from the top plate to the bottom plate in the three-dimensional space of the coal mining area was high-low-high. When $T=100$ s, the dust generated by the hydraulic support shifting and coal cutting was affected by the lateral wind flow on the coal cutter side, and entered the goaf. The dust concentration in the goaf increased rapidly. The concentration at 134 m downwind the coal mining machine remained high. When $T=200\text{--}300$ s, the dust concentration at the front end gradually decreased with increased pollution diffusion range, while dust accumulation still existed on the roadway floor and at the top of the hydraulic support. When $T=400$ s, the dust in the haulageway and sidewalk entered the return airway. The working face was basically filled with dust, which spread in the whole space of the coal mining area, and the dust concentration of the machine tunnel reached its maximum and remained stable. When $T=500\text{--}600$ s, during this time, it can be clearly observed that the dust in the coal mining area was close to saturation. The dust concentration tends to be stable, and the dust concentration in the goaf was in a higher range. The side description shows that the wind speed of air leakage in the goaf was small, and the path of the same air flow was much longer than the air flow inside the machine tunnel. When $T=700$ s, the entire coal mining area and the goaf have almost reached the equilibrium state of dust concentration, and the goaf has been filled with dust. When $T=800$ s, the dust concentration in the coal mining area remains dynamic and stable. The amount of dust entering the goaf and the dust concentration returning to the coal mining area and transportation lane with the wind have also reached a stable state, and the dust concentration in the transportation lane remains at 1200 mg/m^3 . When $T>900$ s, the dust generated by coal cutting, hydraulic support shifting, and the dust returned in the return airway were dynamically stable. The dust concentration was at a higher level in the roadway.

Figures 13 and 14 show that the dust from the coal cutting and hydraulic support shifting was superimposed at the back of the coal cutter and formed a dust cluster more than 2850 mg/m^3 . The dust concentration in the local area of the sidewalk was close to 3700 mg/m^3 , which was the most important dust-proof area in the whole mining process. The area 0–122 m of the downwind sidewalk of the advancing support had a dust concentration of more than 1200 mg/m^3 . Because the wind flow speed remained at 0.4–0.8 m/s at the height of the sidewalk breathing zone, sedimentation along the dust after 122 m was not apparent.

Figures 13 to 15 show that the dust concentration in most places in the haulageway and sidewalk exceeded 1000 mg/m^3 . The blue line of the 0–18-m range on the downwind

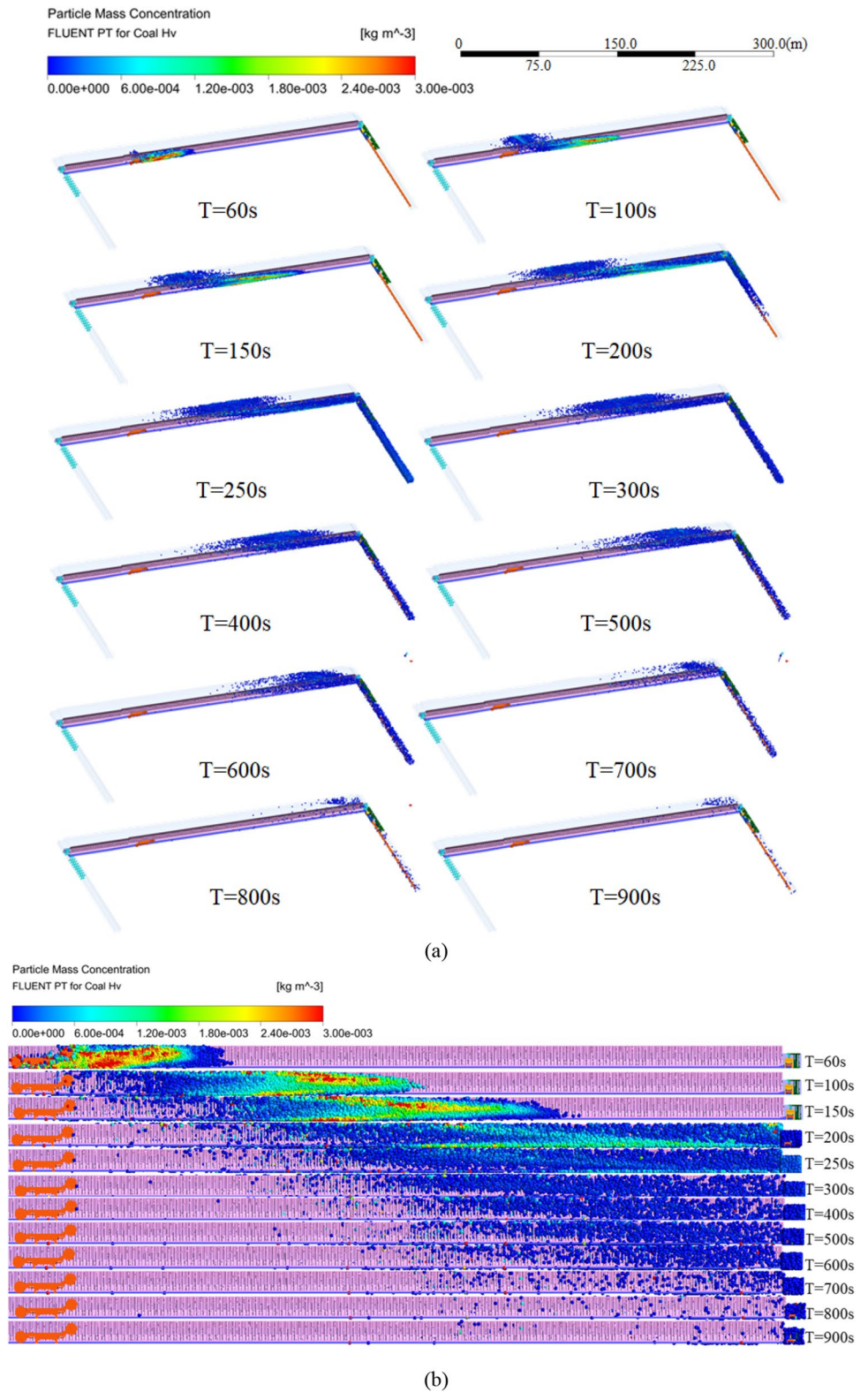
Fig. 11 Laws of dust pollution diffusion in coal cutting for 30 s



side of the advancing support was higher than the red line because the support was closer to the sidewalk than the place

where coal cutting happens, and the dust directly entered the height of the sidewalk breathing zone; at 18–51 m, based on

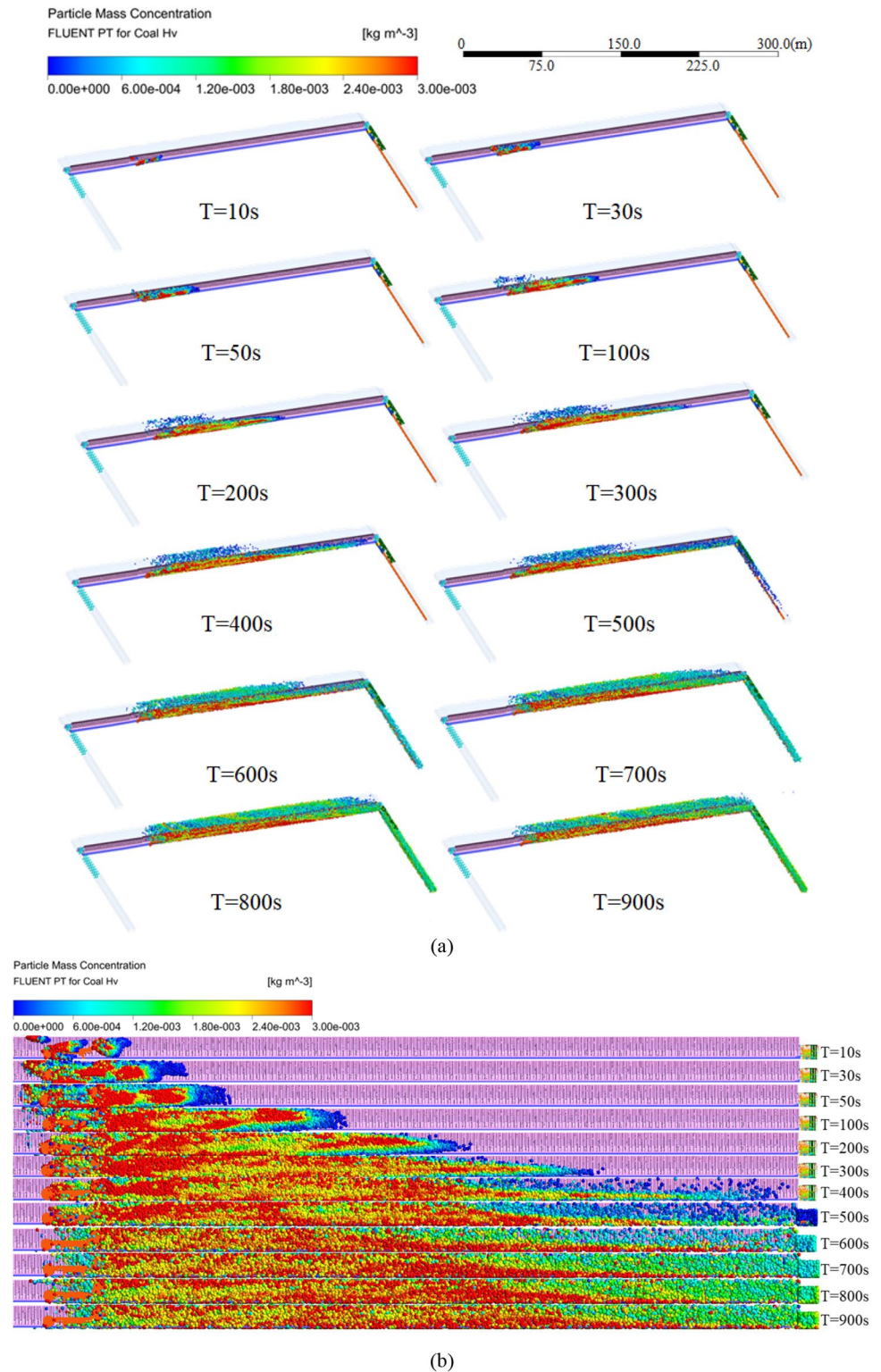
Fig. 12 Laws of dust pollution diffusion in coal cutting for 60 s



the original dust produced by hydraulic support shifting, the horizontal wind flow at the machine brings the coal cutting dust into the sidewalk, and the dust concentration instantly

rises to above 3000 mg/m³. Behind 51 m, the dust in the sidewalk diffused to the goaf, and the dust concentration decreased significantly. In the haulageway, a large amount

Fig. 13 Pollution and diffusion laws produced by continuous coal cutting and shifting



of dust produced by coal cutting continuously moved backward, resulting in the dust concentration decreasing slower than that in the sidewalk. In general, the dust concentration in the sidewalk and the haulageway showed a trend of sudden rise and gradual fall.

Field measurements

To assess the reliability of the numerical simulation results, the actual dust concentration at the No. 22305 fully mechanized mining face in the Bulianta coal mine

Fig. 14 Histogram of high dust concentration in the sidewalk breathing zone

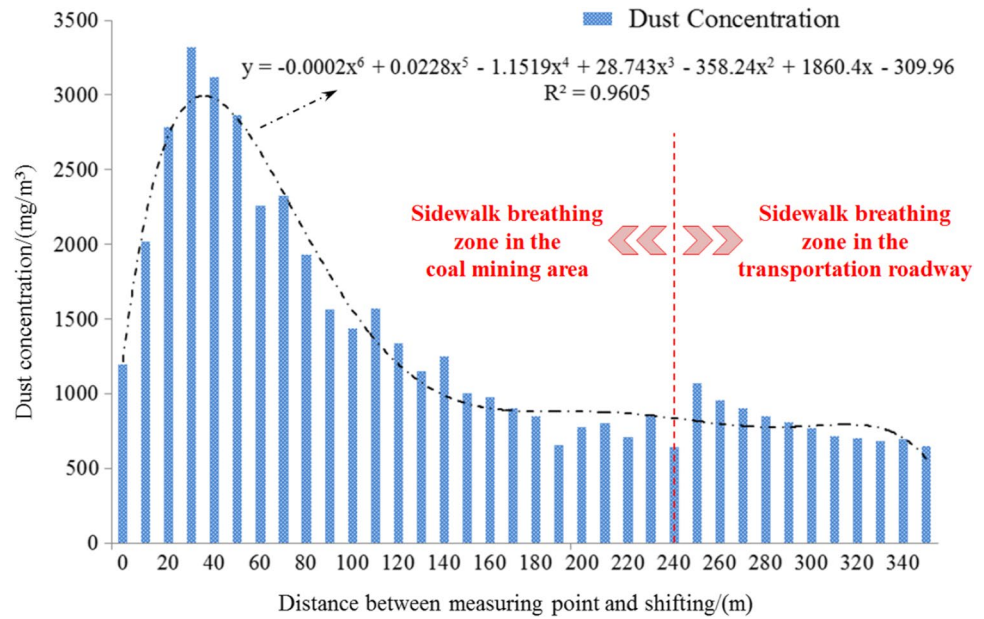
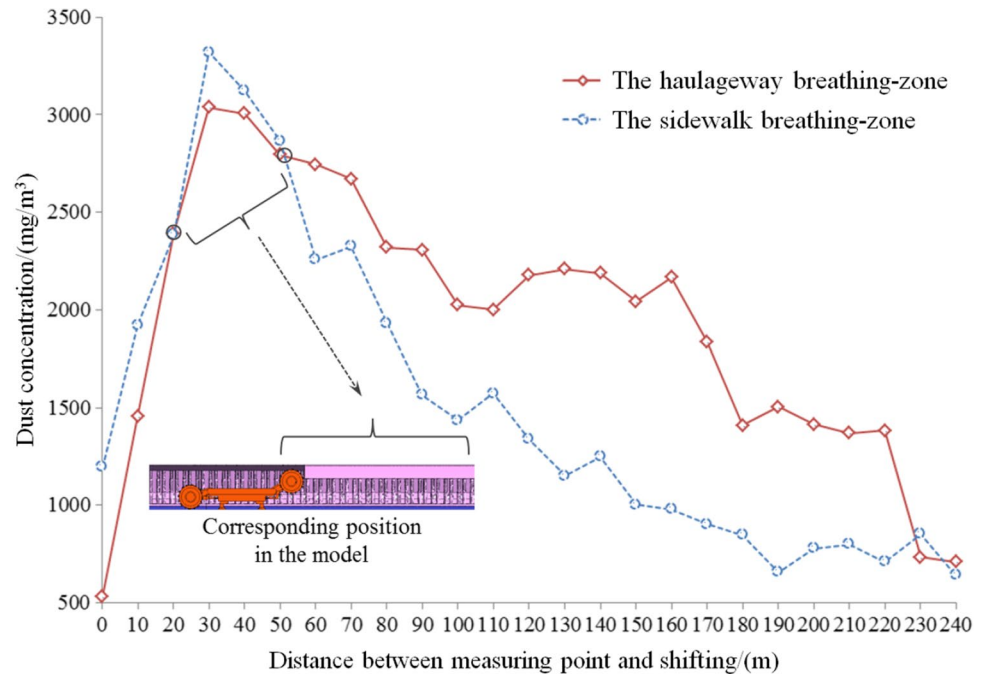


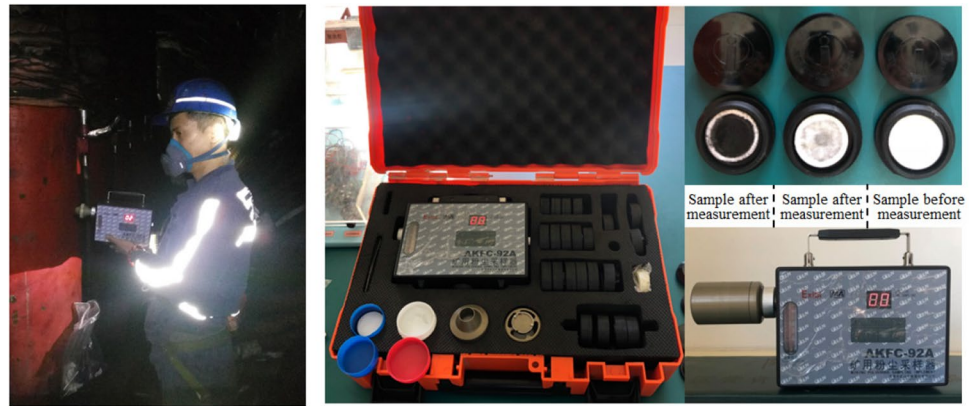
Fig. 15 Dust concentration in the sidewalk and the haulageway breathing zones in the coal mining area



was measured. As shown in Fig. 16, the dust sample was collected using an AKFC-92A mine dust sampler, and the dust concentration was measured. The arrangement of the measuring points was as follows: the dust concentration was measured at 10-m intervals from the advancing support. Each point was measured three times with the arithmetic average value of the three used as the measured result.

Through the comparisons shown in Table 3, we can see that during continuous coal cutting and hydraulic support shifting; differences were observed in the patterns of

dust production: (i) the difference in dust concentration between the dust produced by hydraulic support shifting and coal cutting was substantial; (ii) coal cutting and shifting at the front and rear of the coal cutter makes the dust concentration increase fast. The dust concentration within 37 m in front of the sidewalk in the coal mining area was kept in a relatively high range. Through the simulated and the on-site measured data, the maximum dust concentration was close to 4000 mg/m³ when no dust-proofing measures were used. The variation in trends for the actual measured data and the numerical

Fig. 16 AKFC-92A dust measuring instrument**Table 3** Comparison of numerical simulations and actual measurements of dust concentrations in the sidewalk breathing zone

Measuring points	0	10	20	30	40	50	60	70	80	90	100	110
Simulation results (mg/m ³)	1195	1921	2383	3621	3322	2866	2256	2326	1933	1565	1437	1573
Measurement data (mg/m ³)	991	2227	3008	3929	3478	2961	2455	2039	1858	1422	1391	1354
Error (%)	20.6	13.7	20.8	4.5	7.8	3.2	8.1	14.1	4.0	10.1	3.3	16.2
Measuring points	120	130	140	150	160	170	180	190	200	210	220	230
Simulation results (mg/m ³)	1337	1150	1249	1002	979	902	847	657	779	801	709	852
Measurement data (mg/m ³)	1475	1359	1399	1261	1106	1158	939	754	845	894	936	980
Error (%)	9.4	15.4	10.7	20.5	11.5	22.1	9.8	12.9	7.8	10.4	24.3	13.1
Measuring points	240	250	260	270	280	290	300	310	320	330	340	
Simulation results (mg/m ³)	970	1068	955	902	850	810	769	717	703	684	697	
Measurement data (mg/m ³)	1049	1308	1075	981	734	711	689	687	563	607	610	
Error (%)	7.5	18.3	11.2	8.1	15.8	13.9	11.6	4.4	24.9	12.7	14.3	

simulation results were basically the same. The relative error between the actual measured data and the numerical simulation results was 3.3 to 24.9%; most relative errors were approximately 10%. The existence of errors may be caused by two factors. First, a physical model was constructed that should imitate the real conditions as well as possible; nevertheless, inevitable, small deviations resulted in differences between the numerical simulation results and actual field measurements. Second, the complex environment of the fully mechanized mining face with the large mining height can result in small errors in the actual measurement process. Overall, the error analysis results are acceptable; this proves the validity of the numerical simulation results.

Conclusions

(i) This research established a physical model of a 7-m-high, fully mechanized mining face that imitates the actual on-site. Furthermore, the comparison between the numerical simulations and the measured data showed

that the simulation results are basically consistent with the actual conditions at the coal mine site. Thus, the results can be used as guidance for preventing dust formations in mines.

(ii) The simulation identified three apparent changes of wind flow in the 7-m-high, fully mechanized mining face: at the air-entrance corner, parallel to the coal cutter position, and at the return wind corner. Air leakage was mainly concentrated 10 m downwind of the air-entrance corner and in the gap of the advancing support. The wind flow speed in the haulageway was higher than that in the sidewalk. The wind flow speed at the height of the sidewalk breathing zone was 0.19–2.08 m/s, which decreased first and then increased.

(iii) Based on the simulations of dust production by coal cutting for 5 s, 30 s, and 60 s, continuous coal cutting and hydraulic support shifting, the dust generation, and pollution diffusion laws were investigated from the perspectives of time and space. According to the simulation results, the dust generated by coal cutting and shifting formed a dust cloud with a concentration above 2850 mg/m³ on the downwind side of the coal cutter. This was an important dust source that caused serious dust pollution in the breathing

zone. The breathing zone 0–120 m downwind of the coal cutter with a dust concentration of more than 1700 mg/m³ must be dust-proof, where effective dust reduction methods should be implemented.

Author contribution Dawei Chen: software, formal analysis, writing- original draft preparation, methodology. Wen Nie: conceptualization, writing—reviewing and editing, funding acquisition. Zihao Xiu: visualization, investigation. Bo Yang: data curation. Tao Du: software. Qiang Liu: supervision. Huitian Peng: software, validation.

Funding This work has been funded by the National Natural Science Foundation of China (NO. 52174191 and 51874191), the National Key R&D Program of China (2017YFC0805201), Qingchuang Science and Technology Project of Shandong Province University (2020KJD002), Taishan Scholars Project Special Funding (TS20190935).

Data availability All data generated or analyzed during this study are included in this published article [and its supplementary information files].

Declarations

Ethics approval and consent to participate Not applicable.

Consent for publication Not applicable.

Competing interests The authors declare no competing interests.

References

- Acton PM, Fox JF, Campbell JE, Jones AL, Rowe H, Martin D (2011) Bryson role of soil health in maintaining environmental sustainability of surface coal mining. *Environ Sci Technol* 45:10265–10272
- Ansart R, Ryck AD, Dodds JA, Roudet M, Fabre D, Charru F (2009) Dust emission by powder handling: comparison between numerical analysis and experimental results. *Powder Technol* 190:274–281
- Cai P, Nie W, Hua Y, Wei WL, Jin H (2018) Diffusion and pollution of multisource dusts in a fully mechanized coal face. *Process Saf Environ Prot* 118:93–105
- Camelli FE, Byrne G, Lohner R (2014) Modeling subway air flow using CFD. *Tunn Undergr Sp Technol* 43:20–31
- Chang P, Xu G, Huang JX (2020) Numerical study on DPM dispersion and distribution in an underground development face based on dynamic mesh. *Int J Min Sci Techno* 30:471–475
- Chen DW, Nie W, Cai P, Liu ZQ (2018) The diffusion of dust in a fully-mechanized mining face with a mining height of 7 m and the application of wet dust-collecting nets. *J Clean Prod* 205:463–476
- Cheng W, Yu H, Zhou G, Nie W (2016) The diffusion and pollution mechanisms of airborne dusts in fully-mechanized excavation face at mesoscopic scale based on CFD-DEM. *Process Saf Environ Prot* 104:240–253
- Cheryl MN, Wayne B, Steven S (2009) Wind tunnel simulation of environmental controls on fugitive dust emissions from mine tailings. *Atmos Environ* 43:520–529
- Cundall PA, Strack ODL (2008) A discrete numerical model for granular assemblies. *Geotechnique* 30:331–336
- Elisaveta S, Neda MK, Doncho D, Neda J (2010) Workplace risk assessment (WRA). *Method and Tools in Public health*. Hellweg, Germany, pp 583–606
- Gómez LC, Milioli FE (2003) Numerical study on the influence of various physical parameters over the gas-solid two-phase flow in the 2D riser of a circulating fluidized bed. *Powder Technol* 132:216–225
- Gousseau P, Blocken B, Heijst GJFV (2011) CFD simulation of pollutant dispersion around isolated buildings: on the role of convective and turbulent mass fluxes in the prediction accuracy. *J Hazard Mater* 194:422–434
- Hamid RN, Hassan BT (2013) Development of boundary transfer method in simulation of gas-solid turbulent flow of a riser. *Appl Math Model* 37:2445–2459
- Hu SY, Feng GR, Ren XY, Xu G, Chang P, Wang Z, Zhang YT, Li Z, Gao Q (2016) Numerical study of gas-solid two-phase flow in a coal roadway after blasting. *Adv Powder Technol* 27:1607–1617
- Jo HY, Ahn JH, Jo H (2012) Evaluation of the CO₂ sequestration capacity for coal fly ash using a flow-through column reactor under ambient conditions. *J Hazard Mater* 241:127–136
- Kong Bo, Patel RG, Capeceatro J, Desjardins O, Fox RO (2017) Verification of Eulerian-Eulerian and Eulerian-Lagrangian simulations for fluid-particle flows. *Aiche J* 63:5396–5412
- Krawczyk J (2020) A preliminary study on selected methods of modeling the effect of shearer operation on methane propagation and ventilation at longwalls. *Int J Min Sci Techno* 30:657–682
- Liu CQ, Nie W, Bao Q, Liu Q, Wei CH, Hua Y (2018a) The effects of the pressure outlet's position on the diffusion and pollution of dust in tunnel using a shield tunneling machine. *Energ Buildings* 176:232–245
- Liu J, Zhang R, Song DZ, Wang ZQ (2019) Experimental investigation on occurrence of gassy coal extrusion in coalmine. *Saf Sci* 113:362–371
- Liu Q, Nie W, Hua Y, Peng HT, Liu ZQ (2018b) The effects of the installation position of a multi-radial swirling air-curtain generator on dust diffusion and pollution rules in a fully-mechanized excavation face: a case study. *Powder Technol* 329:371–385
- Lu SG, Chen YY, Shan HD, Bai SQ (2009) Mineralogy and heavy metal leachability of magnetic fractions separated from some Chinese coal fly ashes. *J Hazard Mater* 169:1–3
- Nie W, Wei WL, Ma X, Liu YH, Peng HT, Liu Q (2017) The effects of ventilation parameters on the migration behaviors of head-on dusts in the headingface. *Tunn Undergr Sp Technol* 70:400–408
- Pang JW, Xie JL, Li CT, Hao YJ, Jian J (2017) Study on dust distribution features of high cutting fully-mechanized coal mining face. *Coal Sci Technol* 45:78–83
- Patel RG, Kong B, Capeceatro J, Fox DO (2017) Verification of Eulerian-Eulerian and Eulerian-Lagrangian simulations for turbulent fluid-particle flows. *Aiche J* 63:5396–5412
- Peirano E, Delloume V, Leckner B (2001) Two- or three-dimensional simulations of turbulent gas-solid flows applied to fluidization. *Chem Eng Technol* 56:4787–4799
- Peng HT, Nie W, Cai P, Liu Q, Liu ZQ, Yang SB (2019) Development of a novel wind-assisted centralized spraying dedusting device for dust suppression in a fully mechanized mining face. *Environ Sci Pollut Res* 26:3292–3307
- Pontiggia M, Derudi M, Busini V, Rota R (2009) Hazardous gas dispersion: A CFD model accounting for atmospheric stability classes. *J Hazard Mater* 171:739–747
- Seaman CE, Shahan MR, Beck TW, Mischler SE (2020) Design of a water curtain to reduce accumulations of float coal dust in long-wall returns. *Int J Min Sci Techno* 30:443–447

- Su DWH, Zhang P, Dougherty H, Dyke MV, Kimutis R (2021) Long-wall mining, shale gas production, and underground miner safety and health. *Int J Min Sci Technol* 31:523–529
- Sun B, Cheng WM, Wang JY, Wang H (2018) Effects of turbulent airflow from coal cutting on pollution characteristics of coal dust in fully-mechanized mining face: a case study. *J Clean Prod* 201:308–324
- Torano J, Torno S, Menendez M, Gent M (2011) Auxiliary ventilation in mining roadways driven with roadheaders: validated CFD modeling of dust behavior. *Tunn Undergr Sp Technol* 26:201–210
- Wang H, Nie W, Cheng WM, Liu Q, Jin H (2018) Effects of air volume ratio parameters on air curtain dust suppression in a rock tunnel's fully-mechanized working face. *Adv Powder Technol* 29:230–244
- Wang PF, Gao RZ, Liu RH, Yang FQ (2020) CFD-based optimization of the installation location of the wall-mounted air duct in a fully mechanized excavation face. *Process Saf Environ Prot* 141:234–245
- Wang QG, Wang DM, Wang HT, Liu JN, He F (2016) Experimental study and implementation of a novel internal foam spraying system for roadheaders. *Tunn Undergr Sp Technol* 59:127–133
- Wang X, Liu X, Sun Y, An J, Zhang J, Chen H (2009) Construction schedule simulation of a diversion tunnel based on the optimized ventilation time. *J Hazard Mater* 165:933–943
- Widiatmojo A, Sasaki K, Sugai Y, Suzuki Y, Tanaka H, Uchida K, Matsumoto H (2015) Assessment of air dispersion characteristic in underground mine ventilation: field measurement and numerical evaluation. *Process Saf Environ Prot* 93:173–181
- Xie K, Li W, Zhao W (2010) Coal chemical industry and its sustainable development in China. *Energy* 35:4349–4355
- Xu G, Chen YP, Eksteen J, Xu JL (2018) Surfactant-aided coal dust suppression: a review of evaluation methods and influencing factors. *Sci Total Environ* 639:1060–1076
- Xu MG, Liu XK, Wen XQ, He PC, Zhu ZW (2014) Research of coal mine dust distribution and movement laws on fully-mechanized working face. *J xi'an Univ Sci Technol* 34:533–538
- Yao XW, Li X, Lu GL (2013) Numerical simulation of ventilation flow field and dust field in fully mechanized caving face with large dip angle. *J Mining Saf Environ Prot* 40:40–43
- Yao XW, Lu GL, Xu KL (2015) Numerical simulation of dust generation at different procedures in steeply inclined fully-mechanized caving face. *J China Coal Soc* 40:389–396
- Zhang C, Anadon LD, Mo H, Zhao Z, Liu Z (2014) Water-carbon trade-off in china's coal power industry. *Environ Sci Technol* 48:11082–11089
- Zhang HH, Nie W, Wang HK, Bao Q, Jin H, Liu YH (2018a) Preparation and experimental dust suppression performance characterization of a novel guar gum-modification-based environmentally friendly degradable dust suppressant. *Powder Technol* 339:314–325
- Zhou G, Zhang Q, Bai RN, Fan T, Wang G (2017) The diffusion behavior law of respirable dust at fully mechanized caving face in coal mine: CFD numerical simulation and engineering application. *Process Saf Environ Prot* 106:117–128
- Zhou G, Zhang Q, Bai RN, Xu M, Zhang M (2016) CFD simulation of air-respirable dust coupling migration law at fully mechanized mining face with large mining height. *J China Univ Mining Technol* 45:684–693
- Zhang Q, Zhou G, Qian XM, Yuan MQ, Sun YL, Wang D (2018b) Diffuse pollution characteristics of respirable dust in fully-mechanized mining face under various velocities based on CFD investigation. *J Clean Prod* 184:239–250

Publisher's Note Springer Nature remains neutral with regard to jurisdictional claims in published maps and institutional affiliations.